Supporting information

Highly Efficient Near-Infrared Thermally-Activated Delayed Fluorescence Organic Light-Emitting Diodes with Emission Beyond 800 nm

Jing-Xing Liang,[†a] Yukun Tang,[†b] Xiaofei Wang,[†c] Kai Zhang,[c] Yu-wei Shih,[b] Chia-Hsun Chen,[d] Tien-Lung Chiu,[e] Pei Jin Li,[f] Jiun-Haw Lee,[f] Chuan-Kui Wang,*[c] Chung-Chih Wu*[b] and Jian Fan*[a,g]

[a] *Institute of Functional Nano & Soft Materials (FUNSOM), Jiangsu Key Laboratory for Carbon-Based Functional Materials & Devices, Soochow University, Suzhou, Jiangsu 215123, China*

[b] *Department of Electrical Engineering, Graduate Institute of Electronics Engineering and Graduate Institute of Photonics and Optoelectronics, National Taiwan University Taipei 10617, Taiwan*

[c] *Shandong Province Key Laboratory of Medical Physics and Image Processing Technology, School of Physics and Electronics, Shandong Normal University, 250014 Jinan, China*

[d] *Department of Chemistry, National Taiwan University, Taipei 10617, Taiwan*

[e] *Department of Electrical Engineering, Yuan Ze University, Taoyuan 32003, Taiwan*

[f] *Graduate Institute of Photonics and Optoelectronics and Department of Electrical Engineering, National Taiwan University, Taipei 10617, Taiwan*

[g] *State Key Laboratory of Structural Chemistry, Fujian Institute of Research on Structure of Matter, Chinese Academy of Sciences, Fuzhou, Fujian 35002, China*

E-mail addresses: ckwang@sdnu.edu.cn (C.-K. Wang), wucc@ntu.edu.tw (C.-C. Wu), jianfan@suda.edu.cn (J. Fan).

[†] These authors contribute equally to this work.

General Information

All reactions were performed under nitrogen atmosphere unless otherwise stated. Dry solutions were purified by PURE SOLV (Innovative Technology) purification system. ^{1}H NMR and ^{13}C NMR were recorded on a Bruker 400 MHz at room temperature. Matrix-Assisted Laser Desorption/Ionization Time of Flight Mass Spectrometry (MALDI-TOF-MS) was measured with a Bruker ultraflextreme MALDI-TOF spectrometer. UV-vis absorption spectra were recorded on Cary 60 spectrometer (Agilent Technologies). PL spectra and phosphorescent spectra were recorded on a Hitachi F-4600 fluorescence spectrophotometer. Differential scanning calorimetry (DSC) was performed on a TA DSC 2010 unit at a heating rate of 10 °C min^{-1} under nitrogen. The glass transition temperatures (T_g) were determined from the second heating scan. Thermogravimetric analysis (TGA) was performed on a TA SDT 2960 instrument at a heating rate of 10 °C min^{-1} under nitrogen. Temperature at 5% weight loss was used as the decomposition temperature (T_d). Cyclic voltammetry (CV) was carried out on a CHI600 voltammetric analyzer at room temperature with ferrocenium-ferrocene (Fc$^+$/Fc) as the internal standard. The oxidative scans were performed using 0.1 M n-Bu$_4$NPF$_6$ (TBAPF$_6$) in deoxygenated dichloromethane as the supporting electrolyte. A conventional three-electrode configuration consisting of a Pt-wire counter electrode, an Ag/AgCl reference electrode, and a Glassy-Carbon working electrode was used. The cyclic voltammograms were obtained at a scan rate of 0.1 V s^{-1}.

OLED fabrication and characterization

An ITO-coated glass substrate was used as the bottom anode and aluminum was used as the top cathode. The ITO glass substrate was prepared by the RF sputter deposition. The surface of the substrate was cleaned with detergent, acetone, and deionized water for 15 minutes. Before evaporation, the dried ITO surface was treated by UV-ozone. The organic thin films were deposited by vacuum evaporation under a base pressure of $\leq 3\times10^{-6}$ torr. The deposition rate of organic materials was maintained at 0.1-0.2 nm/s. The current-voltage-radiance (I-V-R) characteristics were measured by a Semiconductor Parameter Analyzer (Agilent) and a goniometric spectroradiometer (DMS, AUTRONIC-MELCHERS GmbH). The external quantum efficiencies of devices were determined with a calibrated integrating-sphere measurement system and by measuring the angular distribution of the emission spectra and intensities.

To determine the emitting dipole orientation in an emitting film, angle-resolved and polarization-resolved PL measurements were performed. The sample consisted of a fused silica substrate with the 30-nm-thick CBP film doped with emitters. The sample was attached to a fused silica half cylinder prism by index matching liquid. The excitation of the samples was performed with the 325-nm line of the continuous-wave He:Cd laser with a fixed excitation angle of 45°. The emission angle was changed by use of an automatic rotation stage. The spectra were resolved by using a p-polarizing filter and were measured by a fiber optical spectrometer. The angle-dependent p-polarized emission intensity at the peak wavelength of the PL spectrum of the emitting layer was detected. The emitting dipole orientation (the horizontal dipole ratio $\Theta_{//}$) was then determined by least square fitting of the measured angle-dependent p-polarized emission intensity with calculated results.

The simulation tool used for the optical simulation of organic layer structures and OLEDs was based on the equivalence between molecular mission through electronic dipole transitions and radiation from classical electrical dipole antenna. With the plane-wave expansion of a dipole field (with each plane-wave mode being characterized by an in-plane wave vector kt), electromagnetic fields generated by a radiation dipole embedded in a layered structure was calculated, from which the distribution of the radiation power into different plane-wave modes and the far-field radiation can be obtained. Emission characteristics of an emitting layer or an OLED are calculated by assuming that the emitting layer contains an ensemble of mutually incoherent dipole radiators with distributions in orientations, locations, and frequencies. The overall emission characteristics and optical out-coupling efficiencies of internally generated radiation into the air were calculated by locating emitting dipoles in the emitting layer and by considering the orientational distribution (using the emitting dipole orientation measured) and the full spectral distribution (using the photoluminescence spectra of emitting layers) of radiating dipoles.

Computational Details

The polarized continuum model (PCM) and a two-layer ONIOM model combined quantum mechanics and molecular mechanics (QM/MM) methods are used to evaluate the photophysical properties of TCN-TPA in toluene and film, respectively. The central molecule is set as a high layer and calculated with QM method, and the surrounding

molecules are treated as a low layer and are considered using MM method with the universal force field (UFF) force field. For the QM calculations, the optimization followed the restricted Kohn−Sham (KS) DFT process, while for singlet excited state, the time-dependent density functional theory (TD-DFT) optimizations are carried out using the restricted KS determinant as reference. In addition, the Tamm-Dancoff Approximation (TDA) is performed to study the triplet excited state. The PBE0-1/3 is adopted in all the following QM calculations in the work. Besides, the 6-31G* basis set is used. All the calculations above are carried out in the Gaussian 16 package.[1] In addition, the transition dipole moment vector and intermolecular interaction are achieved using the wave function analysis software Multiwfn.[2]

Computational Details for MD simulations

All atomic and molecular dynamics simulations are based on the general AMBER force field (GAFF) in the GROMACS-2016.1 package. The charges for TCN-TPA and CBP are obtained by the restrained electrostatic potential (RESP) fitting method. The vdW interactions were computed with a cutoff distance of 1.2 nm. The long-range electrostatic interactions were conducted by the particle-mesh Ewald (PME) method with a cutoff of 1.2 nm. Complete the simulation of TCN-TPA in CBP by the following steps: (1) the initial system was constructed by randomly placing 150 molecules (60 Py-TPA and 90 CBP) in a box (70 × 70 × 70 Å); (2) compression for an initial 5 ns at 600 K and 100 bar to make the molecules close together; (3) another 10 ns simulation at 600 K and 1 bar, then cooling from 600 K down to 298 K gradually within 3 ns; and (4) equilibration simulation for 20 ns at 298 K and 1 bar. The velocity rescaling (V-rescale) thermostat and Berendsen barostat are applied for the temperature and pressure control processes, while for the final 10 ns in the equilibration simulation process, the V-rescale thermostat and the Parrinello–Rahman barostat are used to obtain equilibrium configurations.

Synthetic procedure and characterization
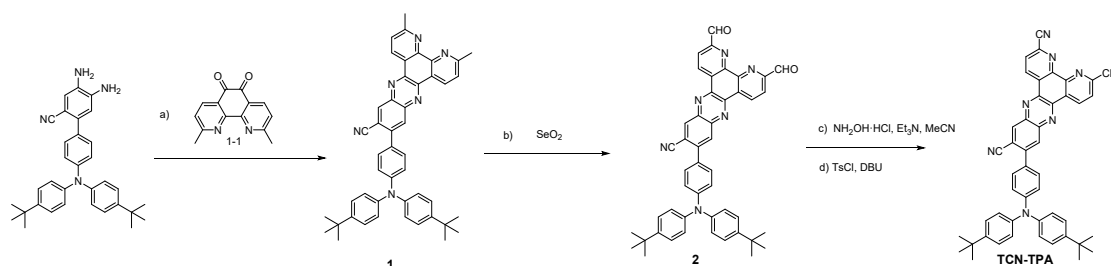
Scheme S1. Synthetic route of TCN-TPA

All reagents were used as received from commercial sources unless otherwise stated. 4,5-diamino-4'-(bis(4-(tert-butyl)phenyl)amino)-[1,1'-biphenyl]-2-carbonitrile and 2,9-dimethyl-1,10-phenanthroline-5,6-dione was synthesized according to the literature method.[3-4]

Synthesis of 12-(4-(bis(4-(tert-butyl)phenyl)amino)phenyl)-3,6-dimethyldipyrido[3,2-a:2',3'-c]phenazine-11-carbonitrile **(1)**:

4,5-diamino-4'-(bis(4-(tert-butyl)phenyl)amino)-4,5-dihydro-[1,1'-biphenyl]-2-carbonitrile (1.5 g, 2.98 mmol), 2,9-dimethyl-1,10-phenanthroline-5,6-dione (782 mg, 3.28 mmol) was suspended in AcOH (120 mL) and heated at 125 °C overnight under nitrogen. After cooling to room temperature, the solution was poured into cold water. The separated solid was filtered off and washed with EtOH several time. and then dried under vacuum to afford the compound **1** (1.68 g, 81.5%). ^{1}HNMR (400 MHz, Chloroform-d) δ 9.49 (dd, J = 8.2, 2.3 Hz, 2H), 8.80 (s, 1H), 8.40 (s, 1H), 7.68 (dd, J = 8.3, 4.0 Hz, 2H), 7.65 – 7.60 (m, 2H), 7.37 – 7.30 (m, 4H), 7.23 – 7.18 (m, 2H), 7.17 – 7.10 (m, 4H), 3.00 (s, 6H), 1.35 (s, 18H). MALDI-TOF-MS: m/z calcd for $C_{47}H_{42}N_6$: 690.347, found: 690.432.

Synthesis of 12-(4-(bis(4-(tert-butyl)phenyl)amino)phenyl)-3,6-diformyldipyrido[3,2-a:2',3'-c]phenazine-11-carbonitrile **(2)**:

Selenium dioxide (592 mg, 5.34mmol) was suspended in 20.5 mL mixture of dioxane and water (20/0.5, v/v) and heated to 90 °C. Compound **1** (1.68 g, 2.42 mmol) was dissolved in 100 mL dioxane and added into the reaction system dropwise. The solution was stirred and heated under reflux for 2 h, and then filtered while hot. The filtrate was dried under vacuum, and then washed with water and DCM. The organic phase was dried under vacuum to afford the compound **2** (1.62 g, 92.9%) ^{1}H NMR (400 MHz, Methylene Chloride-d2) δ 10.51 (d, J = 1.4 Hz, 2H), 9.84 (dd, J = 8.3, 5.9 Hz,

2H), 8.88 (s, 1H), 8.51 – 8.44 (m, 3H), 7.69 – 7.62 (m, 2H), 7.42 – 7.35 (m, 4H), 7.16 (dt, J = 9.2, 2.1 Hz, 6H), 1.35 (s, 18H) MALDI-TOF-MS: m/z calcd for $C_{47}H_{38}N_6O_2$: 718.306, found: 718.365.

Synthesis of 12-(4-(bis(4-(tert-butyl)phenyl)amino)phenyl)dipyrido[3,2-a:2',3'-c]phenazine-3,6,11-tricarbonitrile **(TCN-TPA)**:

Compound **2** (500 mg, 0.69 mmol), hydroxylamine hydrochloride (190 mg, 2.76 mmol) and triethylamine (459 mg, 4.55 mmol) were dissolved in dry acetonitrile (50 mL). The mixture was stirred and heated under reflux overnight. The mixture was allowed to cool to room temperature and then p-toluenesulfonyl chloride (524 mg, 2.76 mmol) and DBU (419 mg, 2.76 mmol) were added into the mixture. The mixture was stirred and heated under reflux for 24 h. After cooling to room temperature, the solvent was removed under reduced pressure, and then the residue was purified by column chromatography with EtOH/DCM (1:30, v/v) to afford the compound **TCN-TPA** (290 mg, 59.1%). ^{1}H NMR (400 MHz, Methylene Chloride-d2) δ 9.81 (dd, J = 8.3, 5.8 Hz, 2H), 8.90 (s, 1H), 8.48 (s, 1H), 8.25 (dd, J = 8.2, 3.3 Hz, 2H), 7.68 – 7.62 (m, 2H), 7.42 – 7.36 (m, 4H), 7.20 – 7.13 (m, 6H), 1.35 (s, 18H). ^{13}C NMR (400 MHz, CDCl$_3$) δ (ppm): 149.95, 148.26, 147.84, 147.25, 145.52, 144.06, 142.40, 140.93, 140.62, 137.67, 136.94, 136.65, 135.85, 135.55, 129.87, 129.70, 129.38, 129.02, 128.93, 128.24, 127.81, 126.43, 125.31, 120.66, 117.73, 116.73, 116.02, 34.45, 31.44. MALDI-TOF-MS: m/z calcd for $C_{47}H_{36}N_8$: 712.306, found: 712.373. HRMS: m/z calcd for $C_{47}H_{36}N_8$: 712.3063, found: 712.3071.
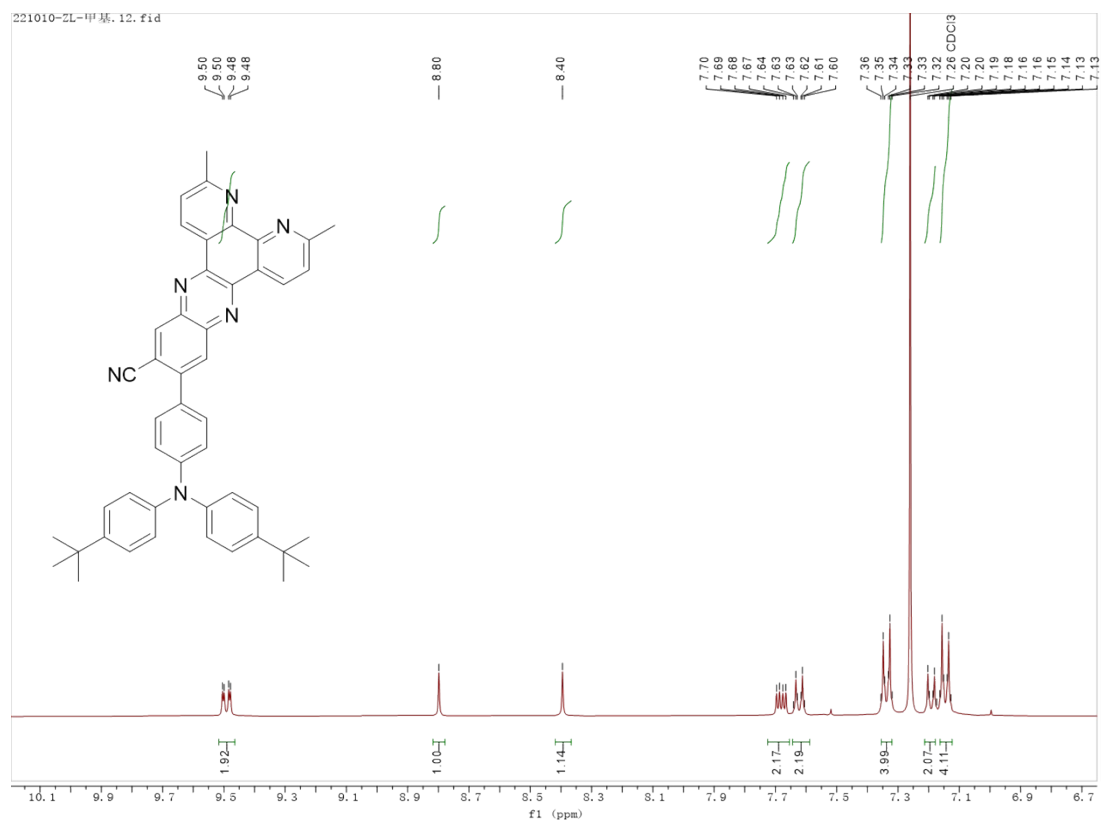
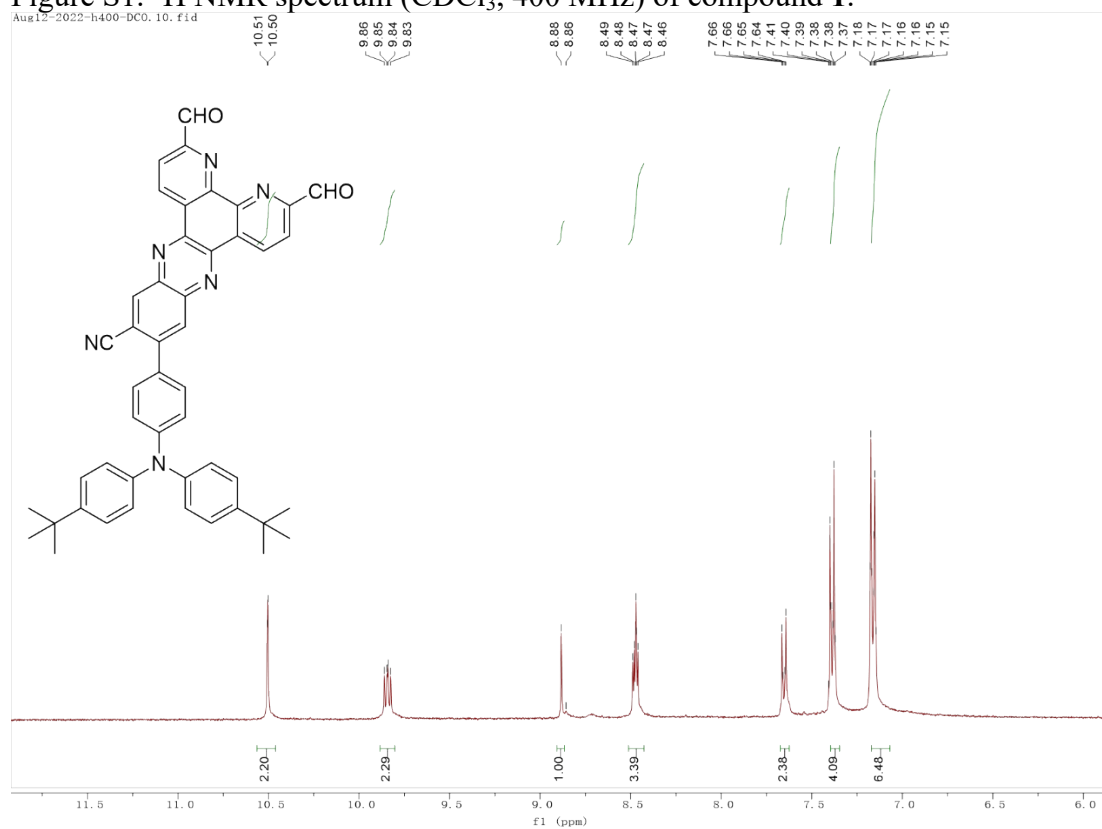Figure S1. ^{1}H NMR spectrum (CDCl$_3$, 400 MHz) of compound **1**.

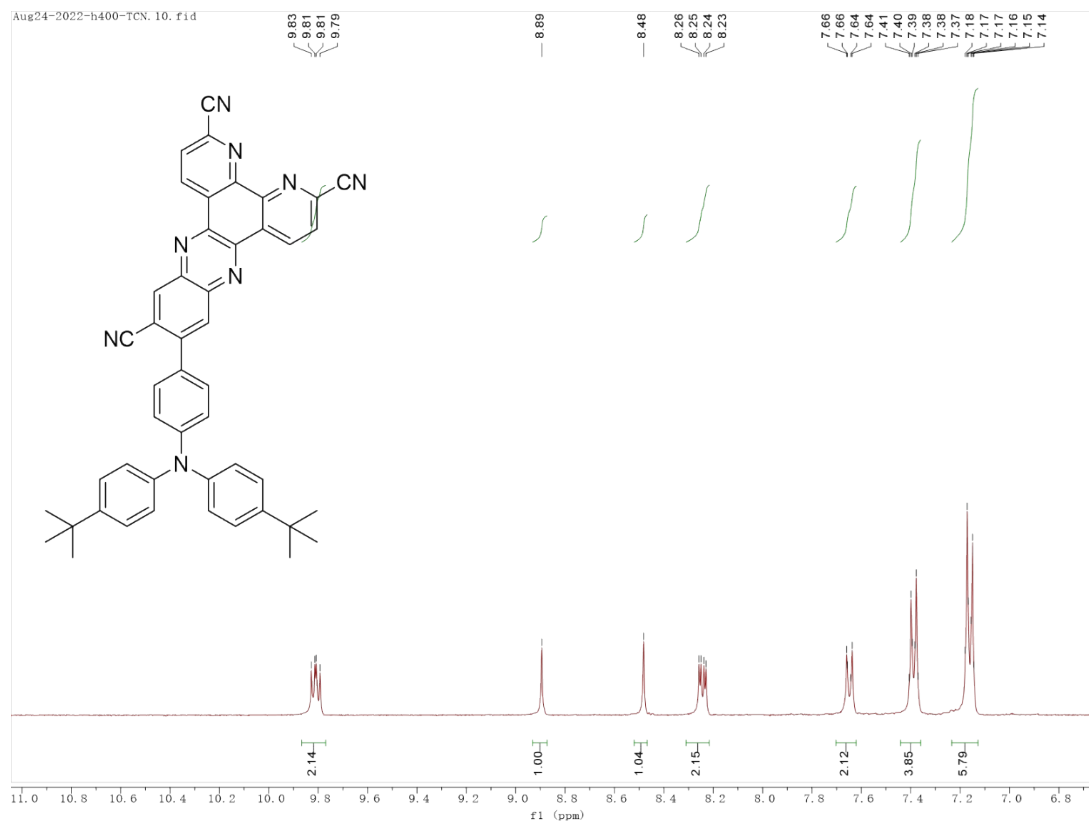Figure S2. ^{1}H NMR spectrum (CD$_2$Cl$_2$, 400MHz) of compound **2**.

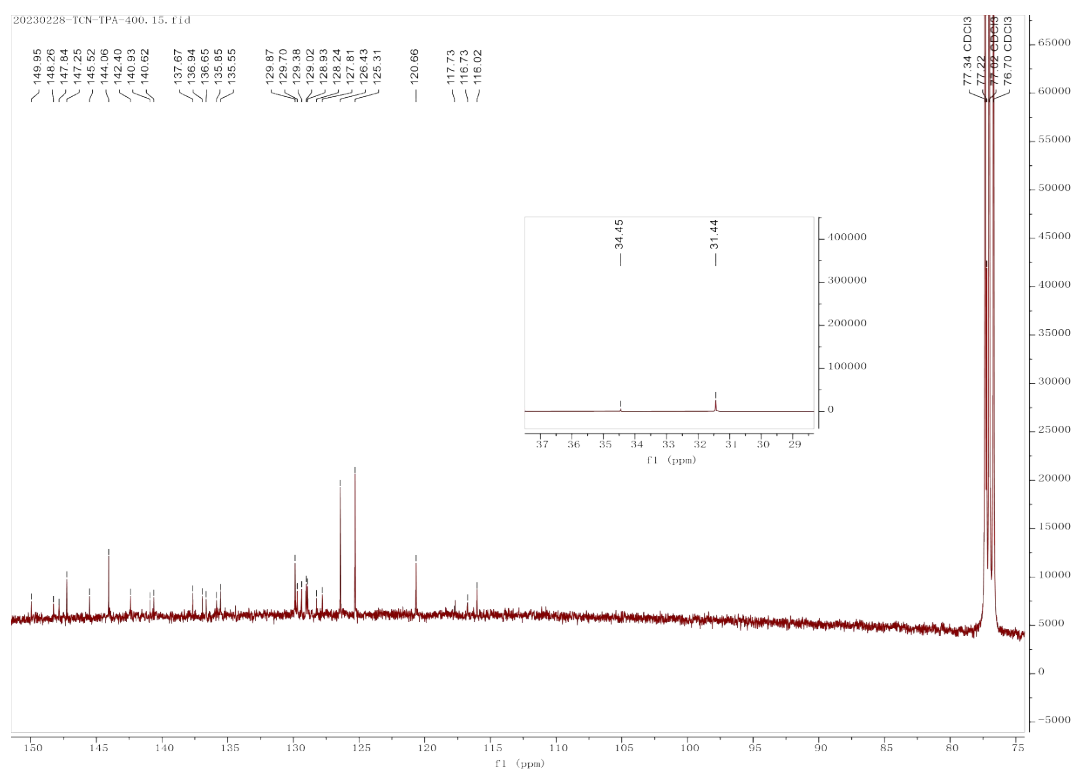Figure S3. ^1H NMR spectrum (CD$_2$Cl$_2$, 400MHz) of **TCN-TPA**.

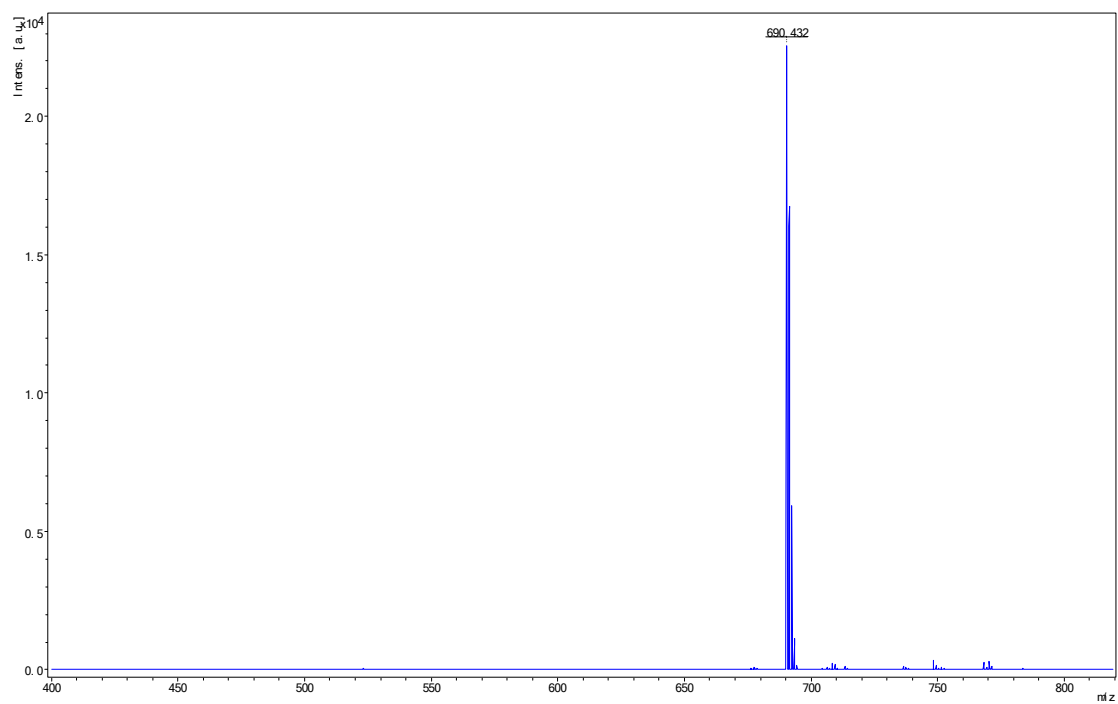Figure S4. ^{13}C NMR spectrum (CDCl$_3$, 400MHz) of **TCN-TPA.**

Figure S5. MALDI-TOF mass spectrum of compound **1**.
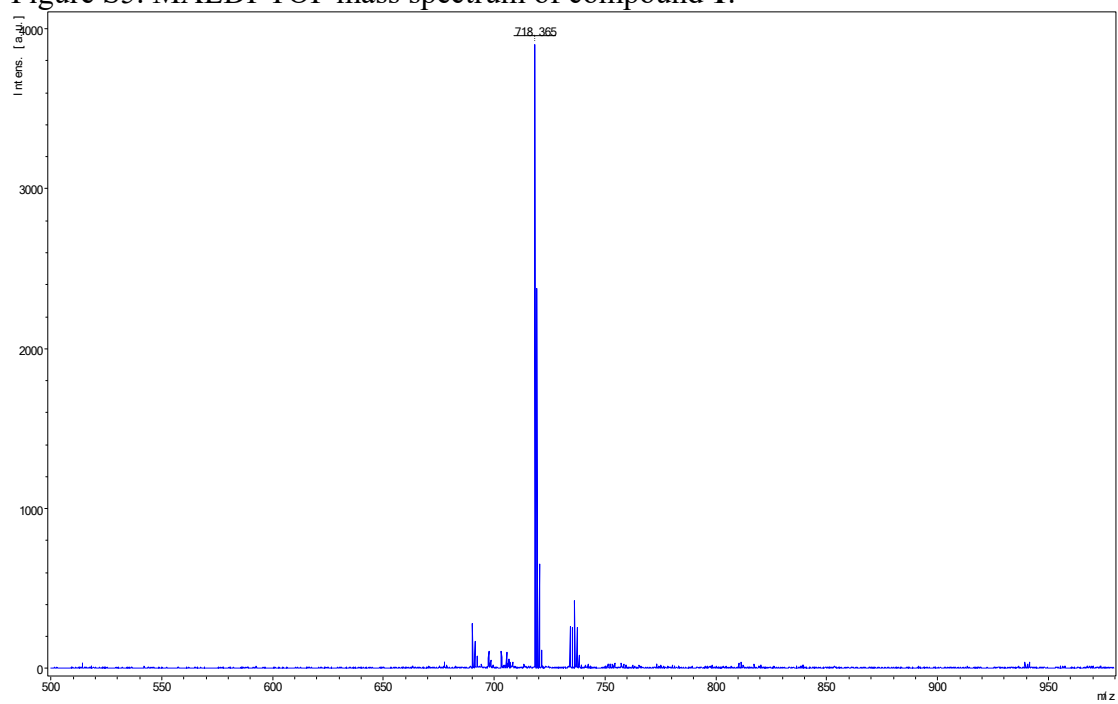
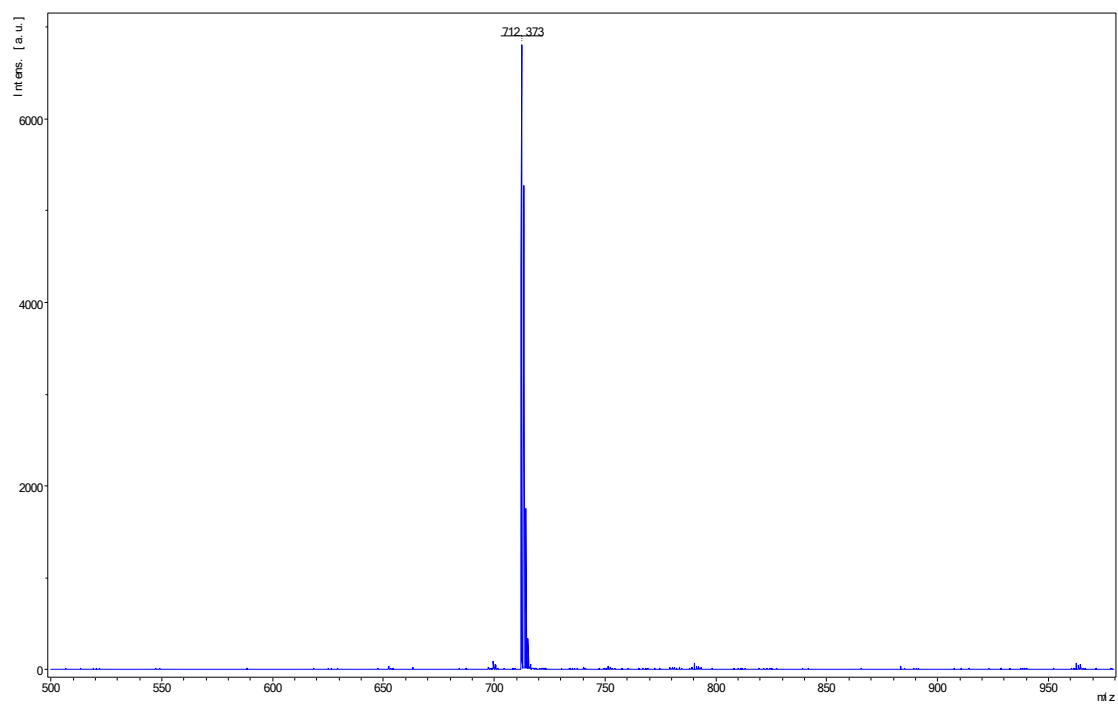Figure S6. MALDI-TOF mass spectrum of compound **2**.

Figure S7. MALDI-TOF mass spectrum of **TCN-TPA**.
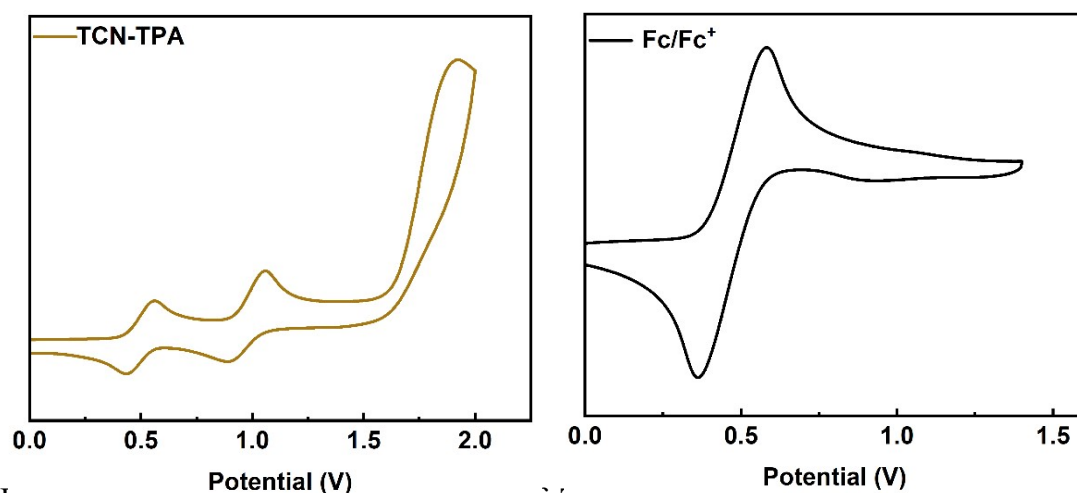
Electrochemical and thermal and properties

Figure S8. **a)** Cyclic voltammograms of TCN-TPA with ferrocene (onset redox potential at around 0.5 V). **b)** Cyclic voltammogram of Fc/Fc⁺.
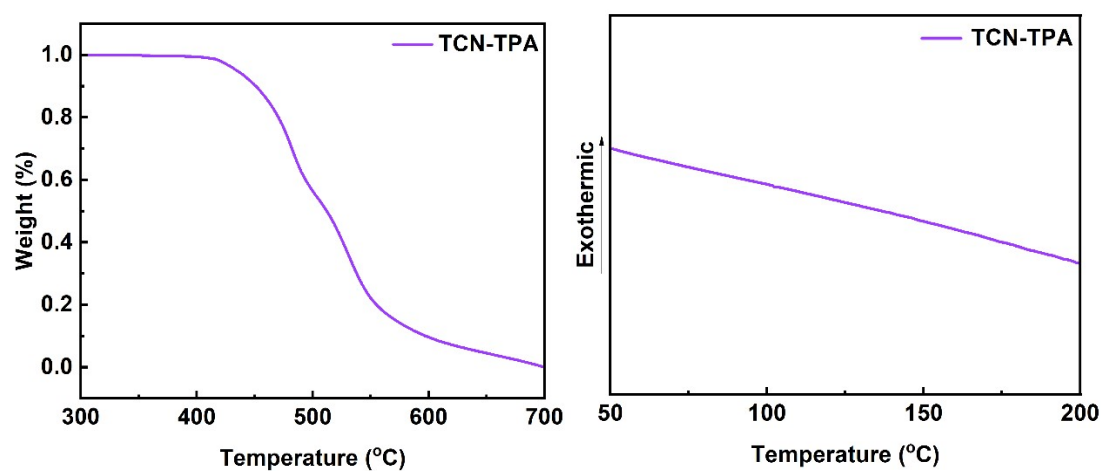

Figure S9. TGA (left) and DSC (right) curves of TCN-TPA at a heating rate of 10 °C/min under N_2.
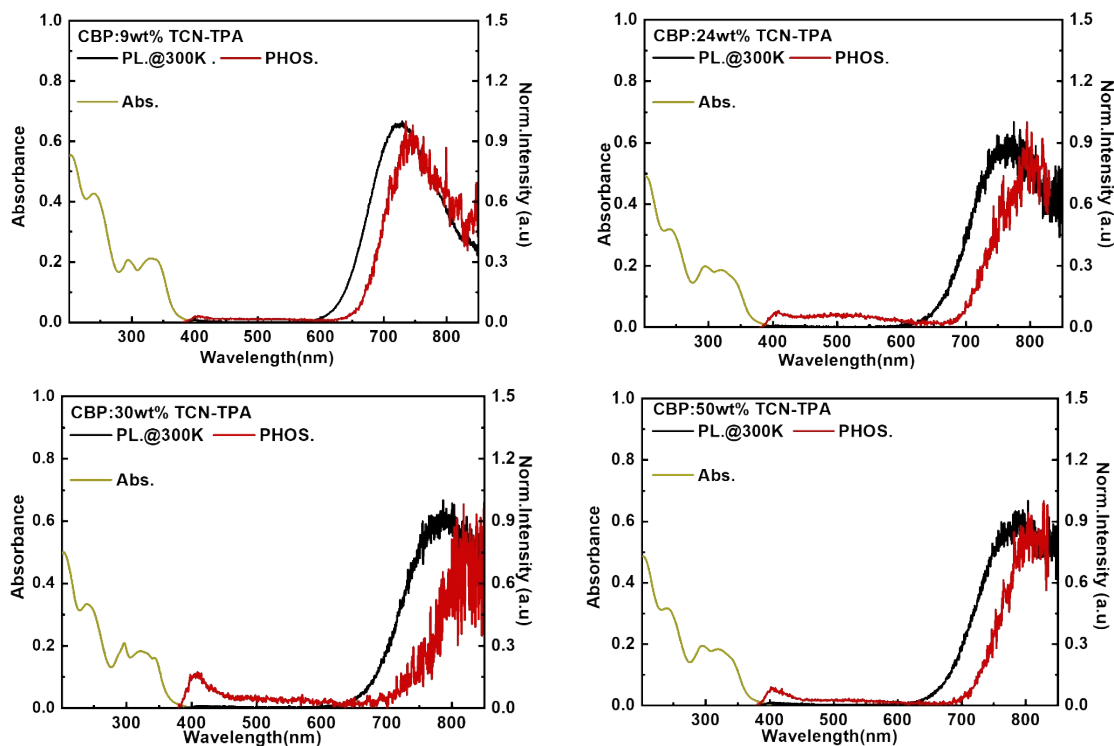
Figure S10. Normalized UV-vis absorption and photoluminescence spectra of TCN-TPA doped CBP host films with different doping concentrations (CBP: x wt% TCN-TPA).
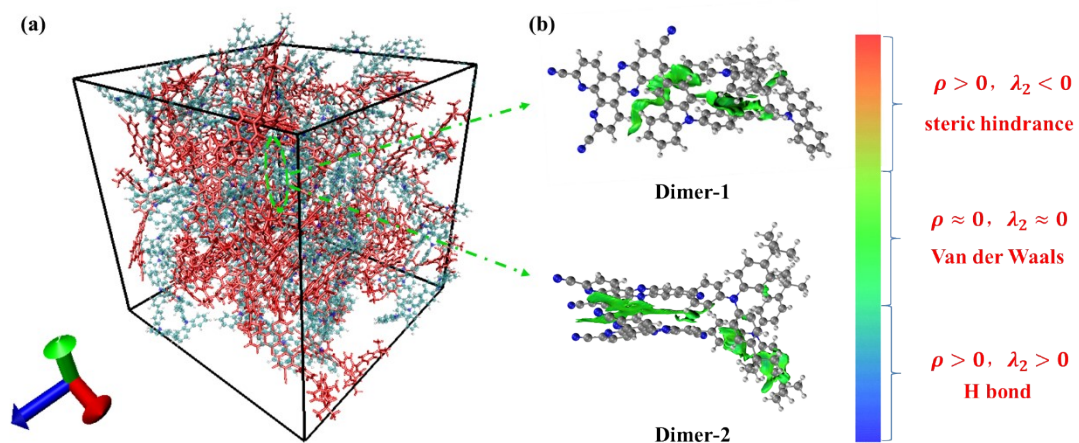
Figure S11. (a) Solid-state structure of TCN-TPA (red) in CBP (cyan). (b) Intermolecular interaction for TCN-TPA in CBP.

Calculation formulas for the photophysical parameters

Ignoring singlet internal conversion (IC) process, the main rate constants were determined by using the following equations:

$\Phi_P = \Phi_{PL} R_P$

$\Phi_d = \Phi_{PL} R_d$

$k_p = 1/\tau_p$

$k_d = \Phi_d/\Phi_{isc}\tau_d$

$k_r^s = \Phi_P k_p$

$\Phi_{PL} = k_r^s/(k_r^s + k_{IC})$

$\Phi_P = k_r^s/(k_r^s + k_{IC} + k_{ISC})$

$\Phi_{IC} = k_{IC}/(k_r^s + k_{IC} + k_{ISC})$

$\Phi_{ISC} = k_{ISC}/(k_r^s + k_{IC} + k_{ISC}) = 1 - \Phi_P - \Phi_{IC}$

$\Phi_{RISC} = \Phi_d/\Phi_{ISC}$

$k_{RISC} = (k_p k_d \Phi_d)/(k_{ISC}\Phi_P)$

R_p and R_d = the ratio of prompt and delayed components; Φ_{PL} is the absolute photoluminescence quantum yield; Φ_p is the prompt fluorescent component of Φ_{PL}; Φ_d is the delayed fluorescent component of Φ_{PL}; τ_p is the lifetime of prompt fluorescent; τ_d is the lifetime of delayed fluorescent; k_p is the rate constant of prompt fluorescence decay; k_d is the rate constant of delayed fluorescence decay; k_r^S is the rate constant of radiative transition from S_1 to S_0; k_{ISC} is the rate constant of intersystem crossing; k_{RISC} is the rate constant of reverse intersystem crossing; k_{IC} internal conversion decay rate from S_1 to S_0 ; Φ_{ISC} is the quantum efficiency of intersystem crossing process.
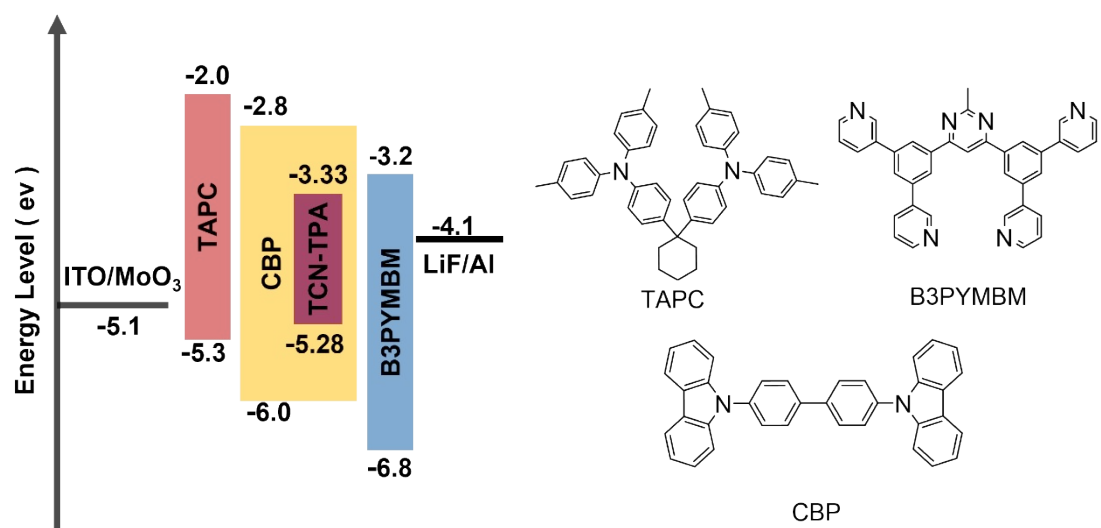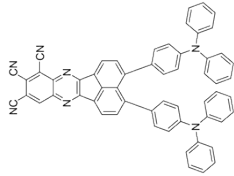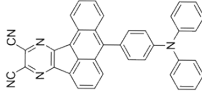
Figure S12. Schematic diagram of the device structure and molecular structures of the materials employed in the devices.

Table S1. Electroluminescence characteristics for the devices based on TCN-TPA.

Emitter	TAPC (nm)	V_{on}[a) (V)	R_{max}[b) [mW/sr·cm²]	CE[c) (cd/A)	PE[d) (lm/W)	EQE[e) (%)	λ_{max}[f) (nm)	Φ_{PL}[g) (%)	CIE[h)(x, y)
TCN-TPA (9wt%)	85	2.2	3.3	0.2	0.1	6.2	756		(0.69, 0.28)
	105	2.2	3.4	0.1	0.1	6.4	758	30.5	(0.71, 0.29)
	125	2.2	2.2	0.1	0.1	5.9	770		(0.68, 0.28)
TCN-TPA (24 wt%)	95	2.0	4.0	0.1	0.1	3.2	775		(0.69, 0.27)
	115	2.0	3.7	0.1	0.1	3.2	784	11.0	(0.66, 0.28)
	135	2.0	2.1	0.1	0.1	3.1	791		(0.68, 0.32)
TCN-TPA (30 wt%)	100	2.0	3.2	0.06	0.03	2.3	785		/
	120	2.0	3.5	0.06	0.03	2.4	802	8.7	/
	140	2.0	3.0	0.06	0.03	2.4	802		/
TCN-TPA (50 wt%)	115	2.0	0.7	0.01	0.01	1.2	838		/
	135	1.8	0.7	0.01	0.01	1.1	841	5.7	/
	155	1.8	0.4	0.01	0.01	1.1	841		/

a) Turn-on voltage with current density $> 10^{-5}$ mA/cm². b) Maximum radiance. c) Maximum current efficiency. d) Maximum power efficiency. e) Maximum external quantum efficiency. f) Electroluminescence peaks. g) Measured at room temperature. h) Commission Internationale de L'Eclairage coordinates.

Table S2 performance of representative near-infrared TADF OLEDs with emission peak between 800 and 900 nm

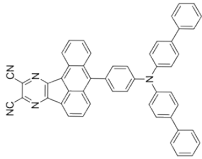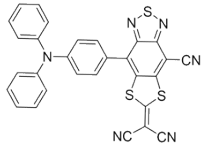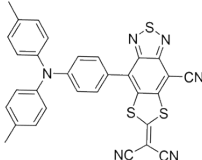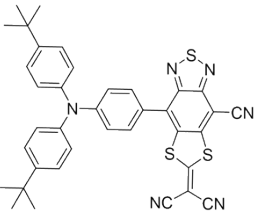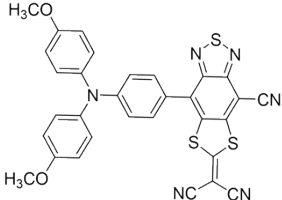| Compound	Chemical structrue	Device configuration	λ_{max} (nm)	EQE (%)	Ref.
AQTC-DTPA		ITO/HAT-CN (10 nm)/TAPC (40 nm)/TCTA (10 nm)/CBP: **60 wt% AQTC-DTPA** (20 nm)/PO-T2T (60 nm)/Liq (2 nm)/Al (120 nm)	810	0.51	5
		ITO/HAT-CN (10 nm)/TAPC (40 nm)/TCTA (10 nm)/CBP: **70 wt% AQTC-DTPA** (20 nm)/PO-T2T (60 nm)/Liq (2 nm)/Al (120 nm)	828	0.41	5
		ITO/HAT-CN (10 nm)/TAPC (40 nm)/TCTA (10 nm)/CBP: **80 wt% AQTC-DTPA** (20 nm)/PO-T2T (60 nm)/Liq (2 nm)/Al (120 nm)	852	0.30	5
		ITO/HAT-CN (10 nm)/ TAPC (40 nm)/TCTA (10 nm)/**AQTC-DTPA** (30 nm)/PO-T2T (60 nm)/Liq (2 nm)/Al (120 nm)	894	0.23	5
DCPA-TPA		ITO/MoO3 (3 nm)/TAPC (40 nm)/TCTA (10 nm)/ **DCPA-TPA** (20 nm)/ POT2T (60 nm)/Liq (2 nm)/Al (120 nm).	838	0.58	6

DCPA-BBPA		ITO/MoO3 (3 nm)/TAPC (40 nm)/TCTA (10 nm)/CBP: 30wt% **DCPA-BBPA** (20 nm)/POT2T (60 nm)/Liq (2 nm)/Al (120 nm).	812	0.50	6
TBSMCN		(ITO)/(m-PEDOT:PSS) (70 nm)/**TBSMCN** (40 nm)/ (DPEPO) (10 nm)/(TmPyPB) (50 nm)/ (Liq) (1 nm)/Al (100 nm)	804	2.17	7
M-TBSMCN		(ITO)/(m-PEDOT:PSS) (70 nm)/**M-TBSMCN** (40 nm)/ (DPEPO) (10 nm)/(TmPyPB) (50 nm)/ (Liq) (1 nm)/Al (100 nm)	862	0.47	7
T-TBSMCN		(ITO)/(m-PEDOT:PSS) (70 nm)/**T-TBSMCN** (40 nm)/ (DPEPO) (10 nm)/(TmPyPB) (50 nm)/ (Liq) (1 nm)/Al (100 nm)	854	0.76	7
O-TBSMCN		(ITO)/(m-PEDOT:PSS) (70 nm)/**O-TBSMCN** (40 nm)/ (DPEPO) (10 nm)/(TmPyPB) (50 nm)/ (Liq) (1 nm)/Al (100 nm)	876	0.022	7

Table S3. Light out-coupling efficiency of the device

Emitter	Doping rate [wt%]	Host	Φ_{out}[%]	exciton utilization efficiency [%][a]
TCN-TPA	9	CBP	34.8	62.0
	24		35.8	84.2
	30		34.2	83.6
	50		33.7	71.0

a) The exciton utilization efficiency is calculated with the equation EQE = EUE × IQE× η_{out}, where IQE is the internal quantum efficiency, EUE is exciton utilization efficiency, and η_{out} is the light out-coupling efficiency.[8]

Reference

[1] Frisch, M. J.; Trucks, G. W.; Schlegel, H. B.; Scuseria, G. E.; Robb, M. A.; Cheeseman, J. R.; Scalmani, G.; Barone, V.; Petersson, G. A.; Nakatsuji, H.; et al. Gaussian 16, Revision A.03; Gaussian, Inc.: Wallingford, CT, 2016.

[2] T. Lu and F. Chen, *J. Comput. Chem*. 2012, **33**, 580-592.

[3] J.-L. He, F.-C. Kong, B. Sun, X.-J. Wang, Q.-S. Tian, J. Fan, L.-S. Liao, *Chem. Eng. J*. 2021, **424**. 130470.

[4] R. H. Zheng, H. C. Guo, H. J. Jiang, K. H. Xu, B. B. Liu, W. L. Sun, Z. Q. Shen, *Chinese Chem. Lett*. 2010, **21**, 1270-1272.

[5] J. F. Cheng, Z. H. Pan, K. Zhang, Y. Zhao, C. K. Wang, L. Ding, M. K. Fung, J. Fan, *Chem. Eng. J*. 2022, **430**, 132744.

[6] Y. J. Yu, Y. Hu, S. Y. Yang, W. Luo, Y. Yuan, C. C. Peng, J. F. Liu, A. Khan, Z. Q. Jiang, L. S. Liao. *Angew. Chem. Int. Ed*. 2020, **59**, 21578.

[7] Y. Yu, H. Xing, D. Liu, M. Zhao, H. H. Y. Sung, I. D. Williams, J. W.Y. Lam, G. Xie, Z. Zhao, B. Z. Tang. *Angew. Chem. Int. Ed*. 2022, **61**, e202204279.

[8] S. Xiao, Y. Gao, R. Wang, H. Liu, W. Li, C. Zhou, S. Xue, S.-T. Zhang, B. Yang, Y. Ma, *Chem. Eng. J*. 2022, **440**, 135911.